Research article

Bifunctional electrocatalytic performance of MgAlCe-LDH/β-Ni(OH)$_2$/Ni foam in total natural seawater splitting

Mahsa Mehravaran, Karim Asadpour-Zeynali [*]

Department of Analytical Chemistry, Faculty of Chemistry, University of Tabriz, Tabriz, 51666-16471, Iran

A B S T R A C T

Electrocatalytic seawater splitting is a potential solution to environmental problems, as seawater is a plentiful supply of hydrogen sources in nature. Hence, the development of bifunctional electrodes exhibiting outstanding performance in both the hydrogen evolution reaction (HER) and the oxygen evolution reaction (OER) is essential for the efficacy of total seawater splitting. Herein, we employed a straightforward method for in situ creation of β-Ni(OH)$_2$ on Ni foam, followed by a hydrothermal approach to manufacture MgAlCe-LDH on β-Ni(OH)$_2$/Ni foam. The linear sweep voltammetry (LSV) experiments demonstrate that the MgAlCe-LDH/β-Ni(OH)$_2$/Ni foam exhibits superior performance for both the OER and the HER in a natural seawater electrolyte compared to the MgAlCe-LDH/Ni foam, β-Ni(OH)$_2$/Ni foam, and Ni foam. Consequently, the MgAlCe-LDH/β-Ni(OH)$_2$/Ni foam requires an 80 mV overpotential for OER and 337 mV for HER to attain a current density of 10 mA cm^{-2}. The enhanced electrocatalytic activity of MgAlCe-LDH/β-Ni(OH)$_2$/Ni foam can be attributed to boosting exposed active sites, improving electronic interaction, and increasing charge transfer capacity resulting from the synthesis of MgAlCe-LDH on β-Ni(OH)$_2$/Ni foam. Implementing a two-electrode configuration for the MgAlCe-LDH/β-Ni(OH)$_2$/Ni foam, the total seawater splitting investigation exhibits 1.42 V cell voltage at a current density of 10 mA cm^{-2} and 25 h long-term stability.

1. Introduction

Worldwide energy and fossil fuel consumption are seeing significant increases caused by population growth and the expansion of industry [1,2]. Uncontrolled fossil fuel consumption caused the current energy crisis and environmental disaster owing to excessive carbon dioxide emissions [3,4]. Fairly recently, to address these issues and to break the cycle of dependency on fossil fuels, certain renewable energy sources have been investigated in order to produce sustainable energy sources [5–7]. Hydrogen (H$_2$), resulting in a specific mass energy of 142 MJ/kg, is considered a pure and viable energy source that has the potential to replace fossil fuels [1,3]. Certain processes, including the reorganization of methane, photovoltaic water decomposition, and fossil fuel extraction, have the potential to produce H$_2$ as a carrier of energy [8]. Nevertheless, electrochemical water splitting is considered an environmentally benign, low-carbon, and minimal-energy method of generating purified H$_2$ [3,9]. Considering the global scarcity of pure water, the production of hydrogen from seawater splitting is significantly more reliable, as oceans and seas comprise approximately 93 percent of the liquid water that exists on Earth [10]. In general, the salinity and pH of seawater fluctuate within the ranges of 3.1–3.8 percent and 7.5–8.4, respectively [10]. Additionally, seawater is composed of a variety of ions, with NaCl being the most prevalent [8,10]. The

---

electrochemical process of water splitting is comprised of two distinct half-reactions, namely oxygen evolution (OER) that occurs at the anode and hydrogen evolution (HER) that takes place at cathode [11]. The redox reaction of water splitting in alkaline environments is implied by equations (1) and (2) [12,13].

$$\text{HER} : 2\,H_2O\,(l) + 2e^- \rightarrow 2OH^-\,(aq) + H_2\,(g)\,\left(E^0 = -0.82\,V\right) \tag{1}$$

$$\text{OER} : \ 2\,OH^-\,(aq) \rightarrow H_2O(l) + 2e^- + \frac{1}{2}O_2\,(g)\,\left(E^0 = -0.40\,V\right) \tag{2}$$

Even though water electrolysis produces hydrogen at the cathode, the stability and efficiency of the OER at the anode significantly influence hydrogen production [8]. However, to attain a sufficient total water splitting reaction (equation (3)), creating effective electrocatalysts that are not noble and demonstrate robust compatibility with both OER and HER simultaneously is of the utmost importance [14].

$$\text{Total reaction} : H_2O \rightarrow H_2 + \frac{1}{2}\,O_2\,\left(E^0 = -1.23\,V\right) \tag{3}$$

The reduction reaction for neutral seawater splitting is thought to be identical to that of alkaline water splitting [13]. However, the oxidation reaction is exceedingly challenging in natural seawater for two reasons: First, it involves multiple proton and electron processes. Second, the OH-oxidation process encounters significant slowing due to the presence of a competing oxidation reaction called the chloride evolution reaction (CER); this is because the two-electron reaction for Cl-oxidation (equation (4)) is more kinetically favorable than the four-electron reaction for OH-oxidation [13,15].

$$\text{CER} : Cl^-\,(aq) + 2OH^-\,(aq) \rightarrow 2ClO^{2-}\,(aq) + H_2O\,(l) + 2e^-\ \left(E^0\ = 0.89\,V\right) \tag{4}$$
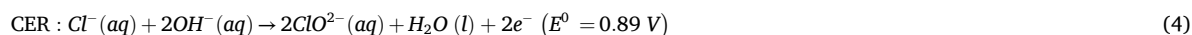
In terms of primary non-noble metals utilized in the development of electrodes for OER and HER, Ni has the highest abundance and lowest price [16]. In alkaline conditions, Hu et al. [11] investigated the electrocatalytic performance of metallic substrates, including Ni foam, Cu foam, Ni mesh, and stainless-steel mesh. Findings showed that among the studied substrates, Ni foam and SS mesh exhibited exceptional performance and stability for HER and OER, respectively. In comparison to NiO, Ni (oxo) hydroxides exhibit superior electrocatalytic efficacy and are significantly more stable than Ni, which easily oxidizes when exposed to oxygen or aqueous solutions [16]. Furthermore, recent studies have shown that Ni (oxo) hydroxides exhibit exceptional activity towards OER [16,17]. Recent energy conversion research is focusing on β-Ni(OH)$_2$ for its eco-friendly features, high theoretical capacitance, cheap cost, and stability in alkaline environments. Yang et al. [17] investigated the bifunctional characteristics of β-Ni (OH)$_2$/Ni foam in total water splitting in 1M KOH, reporting 1.81 V and 1.73 V overpotentials for Ni foam and β-Ni(OH)$_2$/Ni foam for reaching 10 mA cm^{-2} current density.

Recent studies have demonstrated that layered double hydroxide (LDH)-based electrodes have the potential to substantially boost metal corrosion resistance due to their self-healing properties and ability to function as inhibitor containers [18,19]. Liu et al. [20] fabricated NiCo$_2$S$_4$@NiFe-LDH on Ni foam through a three-step hydrothermal route and subsequently studied the performance of prepared electrocatalyst for OER and HER. In their study, intense contact and exchange of charges between NiCo$_2$S$_4$ and NiFe-LDH, which resulted in differences in the surface activity and the facial electronic structure, were responsible for improving OER and then overall water splitting. Iqbal et al. [21] created Ce-dope MgAl-LDH (MgAlCe-LDH) as a co-catalyst with Au nanoparticles to more effectively reduce 4-nitrophenol, and the high catalytic activity of MgAlCe-LDH@Au in the removal of organic contaminants is attributed to the reversible oxidation state of the Ce^{3+}/Ce^{4+}, facilitating a facile exchange of cerium`s oxidation state throughout both oxidation and reduction situations.

In the presented work, we have applied a straightforward one-step approach to create β-Ni(OH)$_2$ on Ni foam at room temperature. Then MgAlCe-LDH nanoparticles with a hydrothermal route were synthesized on β-Ni(OH)$_2$/Ni foam. We evaluate the MgAlCe-LDH/ β-Ni(OH)$_2$/Ni foam electrocatalytic response for OER and HER with a three-electrode system, as well as the dual-functional capability of the MgAlCe-LDH/β-Ni(OH)$_2$/Ni foam with a two-electrode configuration in natural seawater electrolytes. Moreover, this work highlights the utilization of natural seawater as an alternative to fresh water to produce H$_2$, as well as the application of LDH-based electrodes to overcome challenges associated with natural seawater splitting, such as chlorine corrosion.

2. Experimental section

2.1. Materials

The chemicals and materials employed during the present investigation are listed as acetone (C$_3$H$_6$O), aluminum nitrate non-ahydrate (Al(NO$_3$)$_3$·9H$_2$O), cerium nitrate hexahydrate (Ce(NO$_3$)$_3$·6H$_2$O), hydrochloric acid (HCl, 37 %), ethanol (C$_2$H$_6$O, 96 %), magnesium nitrate hexahydrate (Mg (NO$_3$)$_2$. 6H$_2$O), urea [CO(NH$_2$)$_2$], potassium nitrate (KNO$_3$), ammonium persulfate ((NH$_4$)$_2$S$_2$O$_8$), and sodium hydroxide (NaOH) that were acquired from Merck Company in Germany. Moreover, the Ni foam, sourced from Nano Bazar Company in Iran and manufactured in Singapore, has a purity level above 99 %.

2.2. β-Ni (OH)$_2$/Ni foam preparation

To decorate β-Ni(OH)$_2$ on Ni foam, initially, the Ni foam was divided into pieces of (0.5 cm × 0.5 cm) pieces subsequently, it was

cleaned with acetone, ethanol, and deionized water for a duration of 10 min each. Following that, the Ni foam was extracted and submerged in a solution containing NaOH (20 mL, 3 M) and $(NH_4)_2S_2O_8$ (10 mL, 1 M) for 6 h at ambient temperature. The thin coating on the Ni substrate underwent several rinses with distilled water and ethanol then dried in a 150 °C oven (Fanavaran Sahand Azar 250F, Iran) for 6 h [22].

2.3. MgAlCe-LDH/Ni foam and MgAlCe-LDH/β-Ni(OH)$_2$/Ni foam preparation

In order to develop the MgAlCe-LDH/Ni foam electrode, 1.5 mM of Mg $(NO_3)_2 \cdot 6H_2O$, 0.4 mM of Al $(NO_3)_3 \cdot 9H_2O$, 0.1 mM of Ce $(NO_3)_3 \cdot 6H_2O$, and 2.00 g of KNO_3 were dissolved in 20 mL of deionized water. Then, aqueous KOH (2.00 M) solution was put in gradually until the pH reached 10. The obtained solution with bare Ni foam was placed into a 50 mL Teflon-lined stainless-steel autoclave and heated at 120 °C for 10 h in a muffle furnace (Griffin Electric Furnace, Britain). As the chemical synthesis process was finished, the autoclave was cooled to room temperature, the electrode along with the synthesized powders was washed twice with ethanol and distilled water, and dried overnight at 50 °C in an oven [21,23]. Moreover, to generate the MgAlCe-LDH/β-Ni(OH)$_2$/Ni foam electrode, the synthesis process was repeated using fabricated β-Ni(OH)$_2$/Ni foam instead of Ni foam.

2.4. Characterization techniques

X-ray diffractometry (XRD) was employed to conduct the crystalline examination of the electrocatalysts (TONGDA TD-3700, China). Moreover, energy-dispersive X-ray (EDX) analysis and elemental mapping strategies (MIRA3 FESEM, TESCAN, and Czech) have been applied for studying the electrocatalyst's elemental composition. Also, the Fourier-transform infrared spectroscopy (FTIR) method was employed to investigate the main functional group in the sample (BRUKER TENSOR 27, Germany). As well, the surface area and pore structure of the catalyst were determined using the Brunauer-Emmett–Teller (BET) procedures (Belsorp mini II Microtrac Bel Corp, Japan) with N_2 adsorption-desorption at 77 K. Further, transmission electron microscopy (TEM) (LEO 906 Zeiss, Germany) and field emission scanning electron microscopy (FE-SEM) (MIRA3 FESEM, TESCAN, and Czech) were used to examine the morphologies of the generated electrocatalysts.

2.5. Electrochemical investigations

The electrocatalytic performance of fabricated electrocatalysts in both HER and OER was investigated via various electrochemical measurements such as linear sweep voltammetry (LSV), cyclic voltammetry (CV), chronoamperometry (CA) (SAMA 500, Iran), and electrochemical impedance spectroscopy (EIS) (AUTOLABGSTAT30, Netherlands) through a three-electrode configuration [24,25]. However, the two-electrode system was employed to investigate total seawater splitting by utilizing MgAlCe-LDH/β-Ni (OH)$_2$/Ni foam as the anode and cathode electrode [20]. All electrochemical experiments in this work, including HER, OER, and total seawater splitting reactions, were conducted at room temperature in a natural seawater electrolyte (pH = 8.2) sourced from the Caspian Sea, Iran. In this research, the saturated calomel electrode (SCE) was employed as a reference electrode, while the platinum electrode was implemented as a counter electrode. In addition, the Ni foam, the β-Ni(OH)$_2$/Ni foam, MgAlCe-LDH/Ni foam and the MgAlCe-LDH/β-Ni(OH)$_2$/Ni foam was served as the working electrodes. Moreover, the Nernst equation (equation (5)) was used for calibrating all potentials measured in the present study (vs. Hg/Hg$_2$Cl$_2$) to the potential of a reversible hydrogen electrode (RHE) [26].

$$E_{RHE} = E_{SCE} + 0.059 \, pH + E^0_{SCE} \tag{5}$$

Moreover, Equation (6) was used to plot the Tafel plot, which was utilized for calculating the Tafel slope.

$$\eta = a + b \log j \tag{6}$$

The overpotential is marked by η, the current density is denoted by j, and the Tafel slope and constant are represented by a and b, respectively [27].

Furthermore, to study the quantity of energy barriers toward OER and HER, the overpotential was calculated according to the following equations (7) and (8), respectively [28].

$$Overpotential\ (mV) = mesurement\ potential\ (V vs. SCE) + 0.241 + (pH \times 0.059) - 1.229\ (V\ vs. RHE) \times 1000. \tag{7}$$

$$Overpotential\ (mV) = mesurement\ potential\ (V. vs\ SCe) + 0.241 + (0.059 \times pH) - 0\ (V\ vs. RHE) \times 1000. \tag{8}$$

The electrochemical active surface area (ECSA) of manufactured electrocatalysts was calculated through assessing the non-Faradaic double-layer capacitance (C_{dl}) and specific capacitance (C_s), as shown in equation (9) [29].

$$ECSA = C_{dl} \, / \, C_s = (I_{dl} \, / \, v) \, / \, C_s \tag{9}$$

To ascertain the C_{dl}, cyclic voltammetry measurements are conducted at various scan rates, following which the I_{dl} is derived from the midpoint of the potential window. Consequently, by graphing the double layer current in relation to the scan rate, the C_{dl} can be ascertained through an analysis of the slope of the resulting graph. In addition, equation (10) is used for calculation of C_s [29,30].

$$C_s = A/(2 \times m \times v \times dV) \tag{10}$$
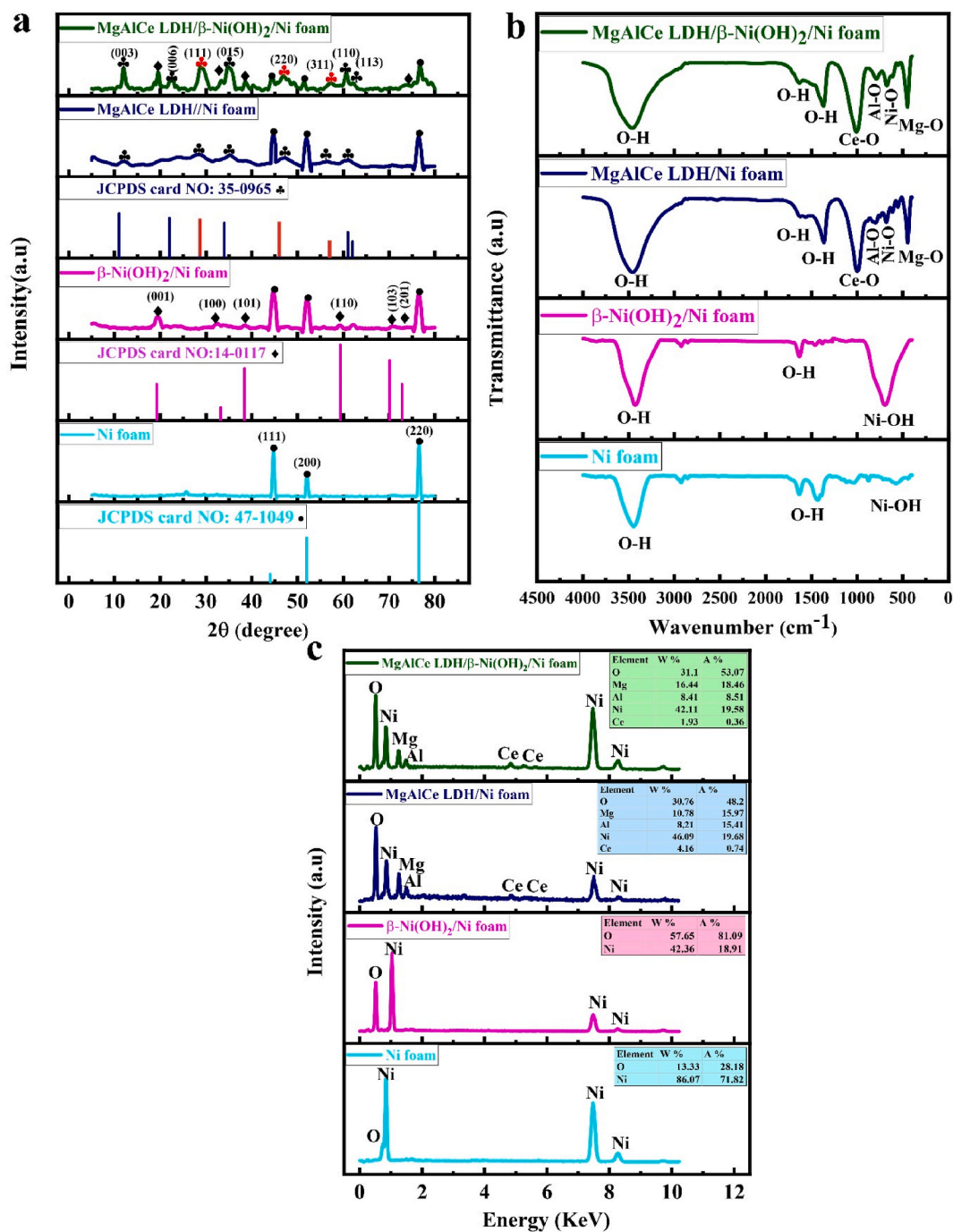
Fig. 1. XRD patterns (a), FT-IR spectras (b), and EDX characterizations of Ni foam, β-Ni(OH)$_2$/Ni foam, MgAlCe-LDH/Ni foam and MgAlCe-LDH/β-Ni(OH)$_2$/Ni foam electrodes.
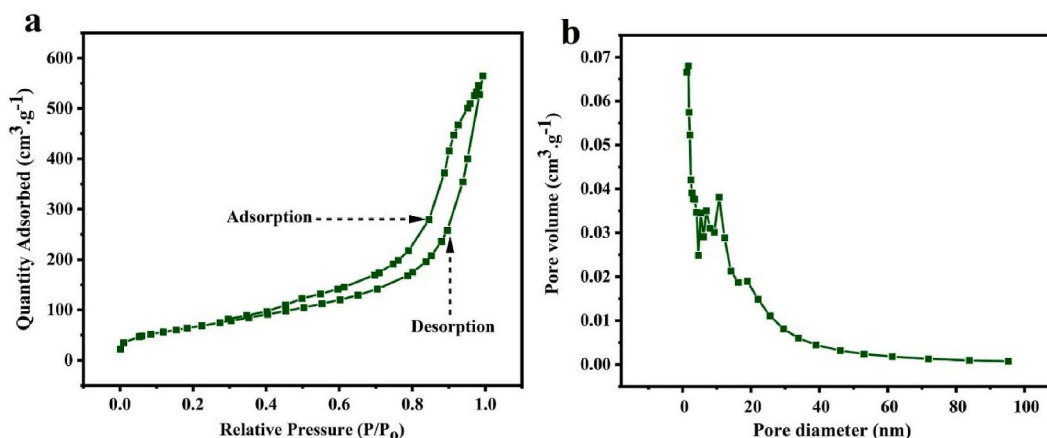
Fig. 2. The N_2 adsorption and desorption isotherms (a) and pore size distribution curve (b) of MgAlCe LDH catalyst.

Table 1
Results of the BET analysis for LDH-based catalysts.

| Catalyst	BET area ($m^2.g^{-1}$)	volume of porous ($cm^3.g^{-1}$)	Average porous size (nm)	Synthesis method	Reference
MgCoAl-CO$_3$-LDH	47.67	0.20	14.65	Ultrasound-assisted coprecipitation	[40]
MgAl-LDH	67.5	0.344	20.4	Hydrothermal	[39]
MgAlCe-LDH	240.8	0.854	14.1	Hydrothermal	This work

Where, *A* represents the area under the curve, *m* denotes the active mass of the electrode, *v* indicates the scan rate, and *dV* signifies the potential window.

3. Results and discussion

3.1. Physical characterization

Fig. 1a illustrates XRD patterns of the prepared electrodes within the diffraction angle ranging from 2θ = 10–80. Three intense peaks were discovered with 2θ angles of 44°, 51.22°, and 76.76°, that are attributed to the (111), (200), and (220) lattice plans of Ni foam according to JCPDS No. 47–1049 [31]. Also, the diffraction peaks at 19.2°, 33.2°, 38°, 51.84°, 59.3°, 62.67°, 70.1°, and 72.8°, which are corresponded to the (001), (100), (101), (102), (110), (111) (103), and (201) planes, are part of the crystal structure of β-Ni (OH)$_2$ based on JCPDS card No. 14–0117 [32]. Moreover, the X-ray diffraction reflects peaks at 11°, 23°, 34°, 60.57°, and 61.11°, which match with (003), (006), (015), (110), and (113) planes are associated with the XRD pattern of MgAl-LDH according to JCPDS card No. 35–0965 [33]. Additionally, according to JCPDS card No. 78–0694, three peaks at 28°, 56.6°, and 47° are attributed to the surface's reflections (111), (311), and (220) belong to Ce (as highlighted with red color on Fig. 1a) [33]. The FT-IR spectrums of the developed electrodes are depicted in Fig. 1b. An extensive absorption peak at a frequency of 3423 cm^{-1} and a distinct absorption peak at 1632 cm^{-1} in the FT-IR spectra of MgAlCe-LDH/Ni foam, MgAlCe-LDH/β-Ni(OH)$_2$/Ni foam, and β-Ni(OH)$_2$/Ni foam is associated with the stretching and bending vibrations of the O-H functional group of absorbed water, respectively [34]. However, atmospheric moisture is responsible for O-H bonding in the FT-IR pattern of Ni foam. In addition, the presence of an absorption peak for O-H bond at 1620 cm^{-1} in FT-IR patterns related to MgAlCe-LDH/Ni foam and MgAlCe-LDH/β-Ni(OH)$_2$/Ni foam is attributed to the LDH structure [33]. Moreover, the vibration of M−O and M−OH bonds is responsible for the occurrence of absorption peaks in the frequency range of 400–1000 cm^{-1} [35]. Consequently, the absorption peaks at 453 cm^{-1}, 572 cm^{-1}, and 796 cm^{-1} are associated with the bonds Mg-O, Ni-OH, and Al-O, respectively [33,34,36]. Also, the Ce-O bond is indicated by an absorption peak at 989 cm^{-1} [37]. Fig. 1c displays the EDX spectra of four manufactured electrodes, along with the atomic and weight percentages of the constituent elements. The presence of the O element in the Ni foam EDX curve may be explained as atmospheric moisture. Furthermore, the EDX patterns of the MgAlCe-LDH/Ni foam and MgAlCe-LDH/β-Ni(OH)$_2$/Ni foam revealed the presence of Mg, Al, and Ce elements, which corroborates the successful deposition of MgAlCe-LDH on Ni foam and β-Ni(OH)$_2$/Ni foam respectively. The atomic ratios of $Mg^{2+}/(Al^{3+}+Ce^{3+})$ and $Ce^{3+}/(Ce^{3+}+Al^{3+})$ were determined to be 2.076 and 0.042, respectively, based on the indicated atomic percentages [38].

The porosity of the synthesized MgAlCe-LDH was characterized by conducting nitrogen adsorption and desorption tests. Fig. 2a presents the nitrogen adsorption and desorption isotherms of MgAlCe-LDH, revealing a form IV isotherm and H$_3$-type hysteresis loop for the catalyst [39]. Fig. 2b depicts the range of pore sizes for fabricated MgAlCe-LDH. According to the BJH approach, the meso-porous form of the synthesized catalyst is confirmed by the highest pore distribution in the 2–50 nm region [33]. Table 1 displays average porous size, complete volume of pore, and BET surface area of MgAl-LDH from previous research in comparison to
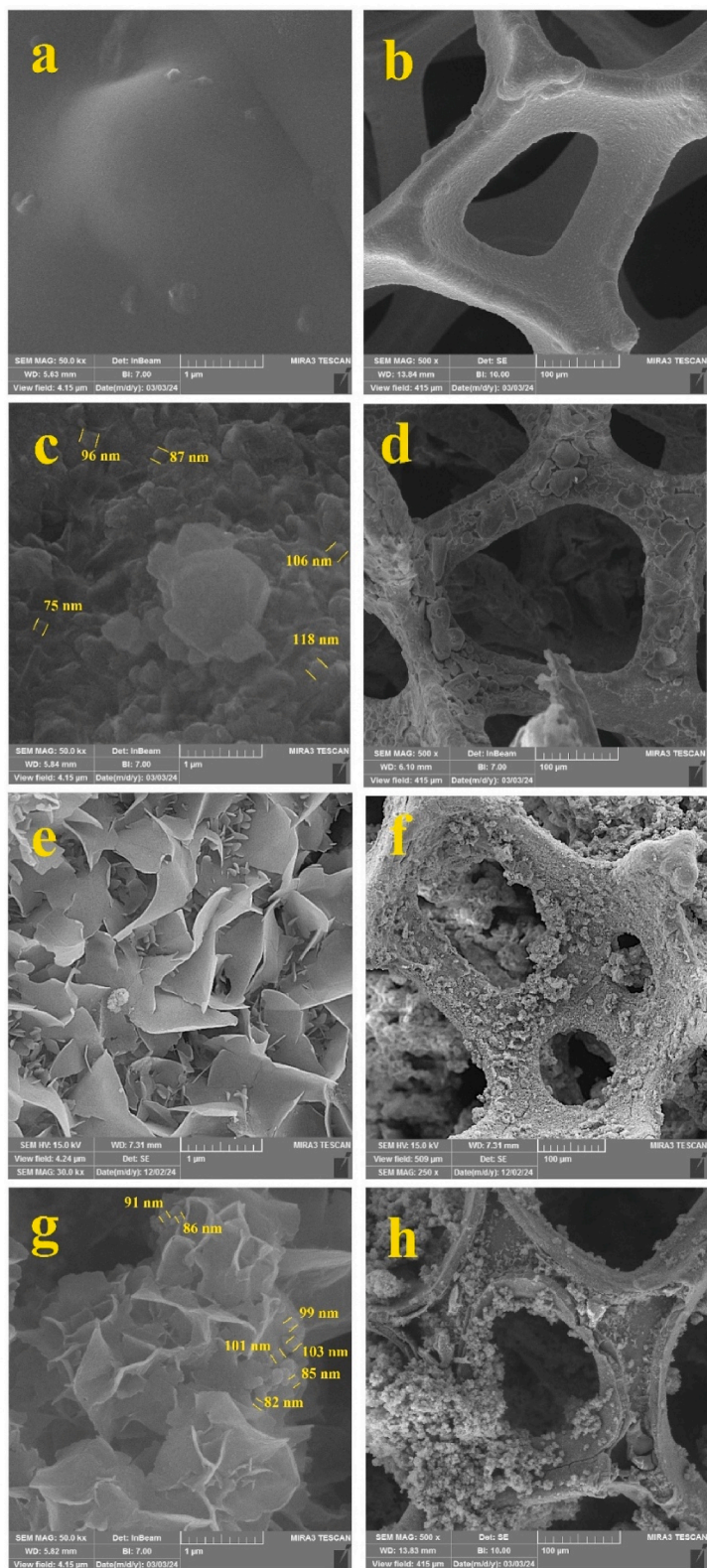
Fig. 3. SEM images of Ni foam (a, b), β-Ni(OH)$_2$/Ni foam (c, d), MgAlCe-LDH/Ni foam (e, f) and MgAlCe-LDH/β-Ni(OH)$_2$/Ni foam (g, h) in the two scales of 1 and 100 μm.
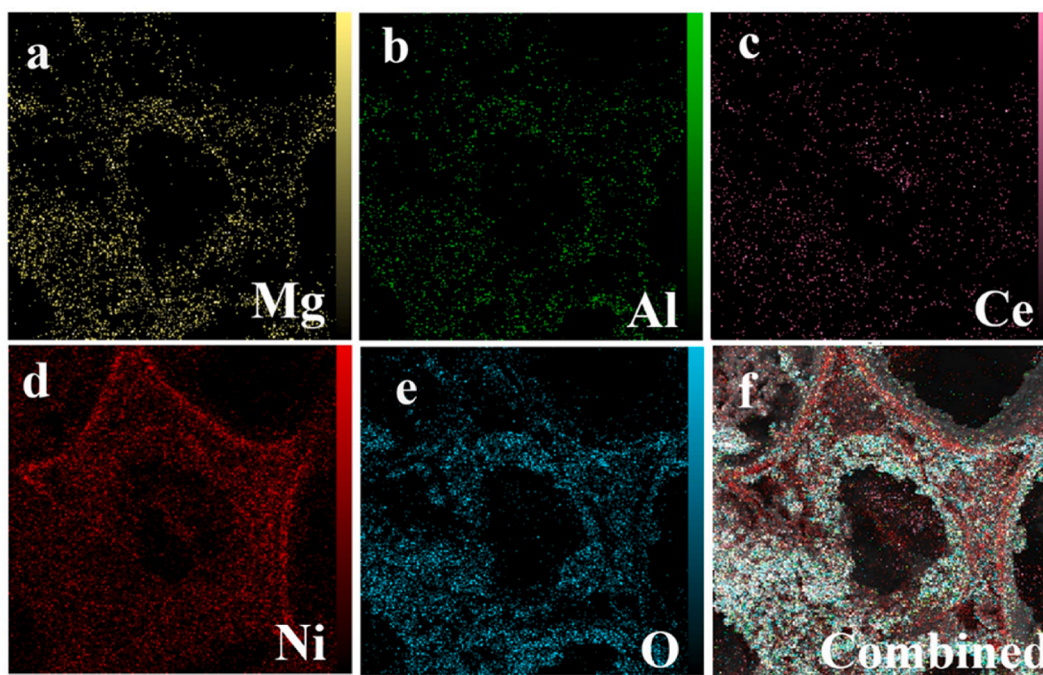
Fig. 4. Mapping analysis of elemental distribution of Mg (a), Al (b), Ce (c), Ni (d), O (e), and combined distribution of elements on Ni foam (f).
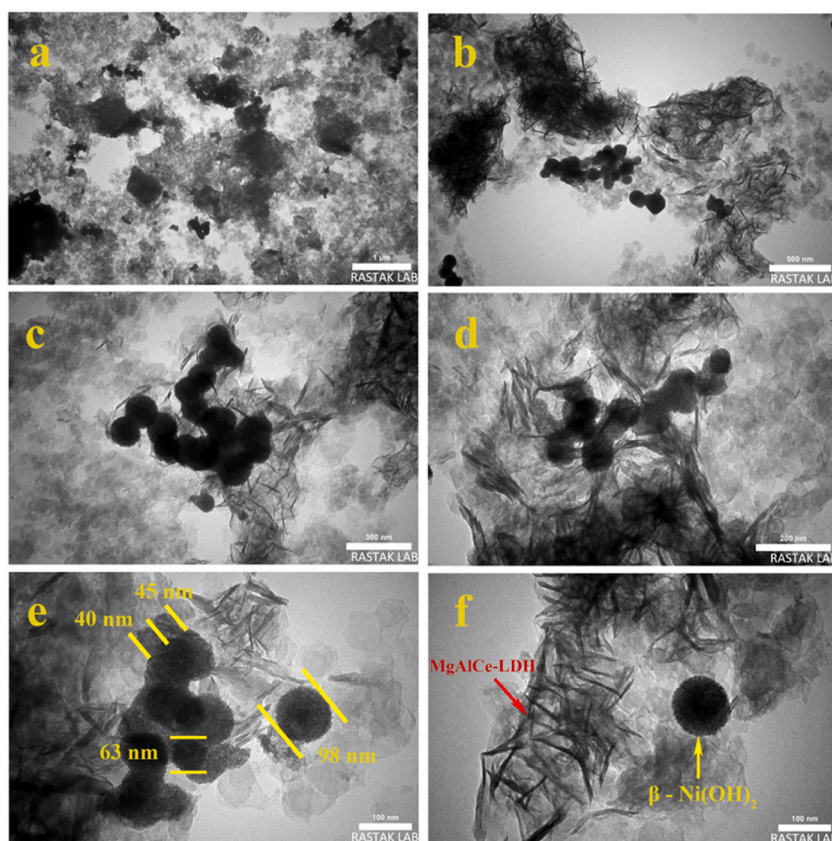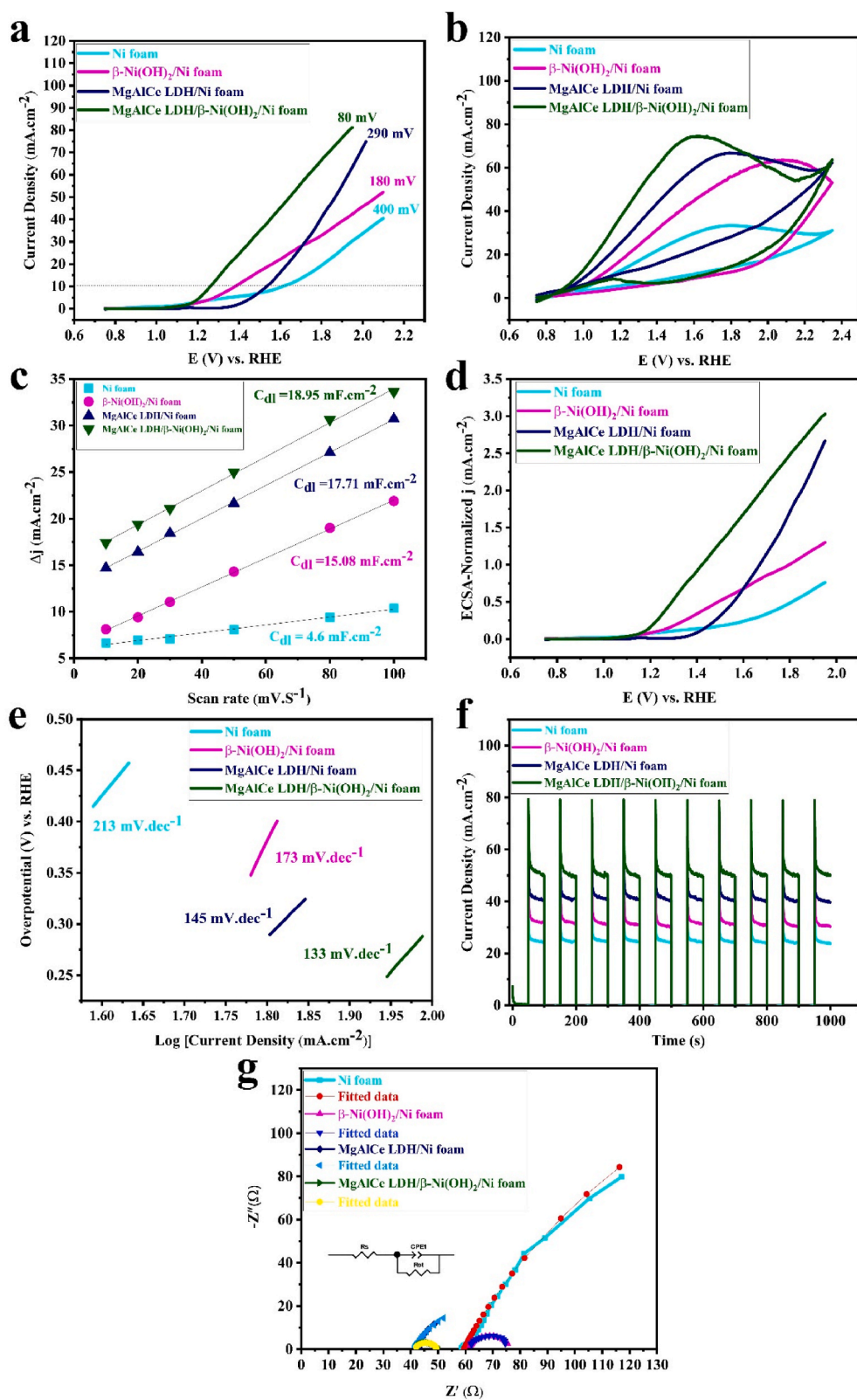

Fig. 5. TEM images of MgAlCe-LDH/β-Ni(OH)$_2$ in the scales of 1 μm (a), 500 nm (b), 300 nm (c), 200 nm (d), and 100 nm (e, f).

Fig. 6. LSV (a), CV (b), Cdl (c), ECSA-Normalized LSV (d), Tafel slope (e), chronoamperometry (f) and EIS (g) curves of the electrocatalysts for OER in natural seawater electrolyte.

Table 2
Fitting values of the EIS assessment during OER in seawater (pH = 8.2) electrolyte at a potential of 1.2 V vs. SCE at room temperature.

Electrocatalyst	Rs (Ω)	CPE	R_{ct} (Ω)	Fitting error
Ni foam	59.39	0.78	46.49	0.008
β-Ni(OH)$_2$/Ni foam	61.14	0.85	15.75	0.007
MgAlCe-LDH/Ni foam	41.4	0.73	10.93	0.004
MgAlCe-LDH/β-Ni(OH)$_2$/Ni foam	41.6	0.84	8.07	0.006

MgAlCe-LDH from this study. The redox performance of the electrocatalyst could be enhanced by increasing the surface area of the MgAlCe-LDH [33].

3.2. Morphological characterizations

Fig. 3 illustrates the morphology and structure of the Ni foam, β-Ni(OH)$_2$/Ni foam, MgAlCe-LDH/Ni foam, and MgAlCe-LDH/β-Ni(OH)$_2$/Ni foam using the FE-SEM technique at scales of 1 μm and 100 μm.Fig. 3a and b demonstrate the Ni foam skeleton's homogeneous and smooth surface [41]. In Fig. 3c and d, the fabrication of β-Ni(OH)$_2$ on the Ni foam surface results in creating rugged surface besides sphere-shaped particles that facilitates rapid passage of electrolytes through the electrode, thereby accelerating the speed of mass transfer [42]. The presence of a layered structure in Fig. 3e is excellent evidence of the successful synthesis of the MgAlCe-LDH. Fig. 3f exhibits a complete coating of Ni foam with MgAlCe-LDH. Furthermore, the FE-SEM images of the MgAl-Ce-LDH/β-Ni(OH)$_2$/Ni foam clearly show the presence of β-Ni(OH)$_2$ particles in the shape of spheres beside the layered structure of the MgAlCe-LDH, as represented in Fig. 3g and h. Additionally, the FE-SEM mapping technique with a 100 μm scale was used to determine the pattern of distribution and abundance of the Mg, Al, Ce, Ni, and O elements that formed over the Ni foam, as depicted in Fig. 4a to e. As illustrated in Fig. 4f, the Ni foam skeleton, which was previously coated by β-Ni(OH)$_2$, is completely covered by MgAlCe-LDH nanoparticles.

The transmission electron microscopy (TEM) technique was utilized to explore the structure and morphology of the prepared catalyst at several scales of 1 μm as well as 500, 300, 200, and 100 nm, as illustrated in Fig. 5. The TEM images presented in Fig. 5a and b illustrate a significant aggregation of two distinct morphologies. Additionally, the TEM images in Fig. 5c and d clearly illustrate spherical particles of β-Ni(OH)$_2$ covered by a layered structure of MgAlCe-LDH [43]. TEM images presented in Fig. 5e and f exhibit a strong correlation with the SEM images obtained from the surface of the MgAlCe- LDH/β-Ni(OH)$_2$/Ni foam.

3.3. OER performance of electrodes

In a natural seawater electrolyte, the OER electrocatalytic efficacy of bare Ni foam, β-Ni(OH)₂/Ni foam, MgAlCe-LDH/Ni foam, and MgAlCe-LDH/β-Ni(OH)$_2$/Ni foam was assessed via a system consisting of three electrodes. The LSV curves of the developed electrodes are depicted in Fig. 6a, with a scan rate of 5 mV s^{-1} and the potential window ranging from 0 to 1.8 V vs. SCE. According to the LSV curves, the growth of β-Ni(OH)$_2$ on Ni foam led to a 2.2 times decrease in overpotential and a 1.6 times increase in the current density of Ni foam. On the other hand, the development of MgAlCe-LDH on Ni foam caused to a 1.37-fold decrease in the overpotential and a 2.33-fold rise in the current density of bare Ni foam. The recorded current density in OER for MgAlCe-LDH/β-Ni(OH)$_2$/Ni foam is 2.28, 1.9 and 1.14 times as large as Ni foam, β-Ni(OH)$_2$/Ni foam and MgAlCe-LDH/Ni foam respectively. However, to be able to create a current density of 10 mA cm^{-2}, the MgAlCe-LDH/β-Ni(OH)$_2$/Ni foam requires 80 mV overpotential, which is much smaller than the energy barriers for MgAlCe-LDH/Ni foam (290 mV), β-Ni(OH)$_2$/Ni foam (180 mV), and Ni foam (400 mV). Comparable findings from Niu et al. [44] investigation into the catalytic performance of the α-FeOOH/β-Ni(OH)$_2$ supported on Ni foam in OER demonstrated that composite material can exhibit a greatly improved OER activity with an especially minimal overpotential. This enhanced performance is attributed to the beneficial interaction of the Ni and Fe species, as well as the formation of an interface within β-Ni(OH)$_2$ and α-FeOOH. As shown in Fig. 6b, to probe the OER electrocatalytic responses of manufactured electrodes, CV curves were captured in a seawater electrolyte and in a three-electrode system with a scanning rate of 100 mV s^{-1} and in a potential variation of 0–1.8 V vs. SCE. According to CV graphs, the significant current density of the MgAlCe-LDH/β-Ni(OH)$_2$/Ni foam electrode compared to the three electrodes evidences its higher electroactivity and conductivity in OER. In the ECSA studies of manufactured electrocatalysts, CV tests were conducted at six distinct scan rates; hence, the C_{dl} of the generated electrocatalysts was ascertained from the slope obtained by plotting non-faradaic current against scan rate, as shown in Fig. 6c [45]. Therefore, the C_{dl} of the MgAlCe-LDH/β-Ni(OH)₂/Ni foam has been determined to be 18.95 mF cm^{-2}, which exceeds the values recorded for the MgAlCe-LDH/Ni foam (17.71 mF cm^{-2}), β-Ni(OH)₂/Ni foam (15.08 mF cm^{-2}), and Ni foam (4.6 mF cm^{-2}). Obtaining larger C_{dl} for the MgAlCe-LDH/β-Ni(OH)$_2$/Ni foam is a manifestation of its more electrochemically active sites, that effectively accelerate OER reaction kinetics [46]. The same result was reported by Yang et al. [47] a 5.08-fold increase in C_{dl} for CuO@CoFe-LDH/Cu foam during seawater oxidation compared to CoFe-LDH/Cu foam, which is related to its enhanced active surfaces. To further investigate intrinsic catalytic performance, the current density of generated electrocatalysts was normalized by calculated ECSA as depicted in Fig. 6d [48]. The superior ECSA value observed for MgAlCe-LDH/β-Ni(OH)$_2$/Ni foam, in comparison to MgAlCe-LDH/Ni foam and β-Ni(OH)$_2$/Ni foam, suggests that its elevated surface density contributes significantly to enhanced performance in the OER [46,48]. Moreover, the Tafel slopes for MgAl-Ce-LDH/β-Ni(OH)$_2$/Ni foam, MgAlCe-LDH/Ni foam, β-Ni(OH)$_2$/Ni foam, and Ni foam were determined to be around 133, 145, 173, and 213 mV.dec^{-1}, respectively, as shown in Fig. 6e. The obtained data reveal that the MgAlCe-LDH/β-Ni(OH)$_2$/Ni foam exhibits the

Table 3

A comparative evaluation of the OER performances of different electrocatalysts supported on Ni foam.

| Electrode	Electrolyte	Overpotential OER (mV)	Cdl (mF. cm^{-2})	Tafel slope (mV. dec^{-1})	Current density (mA. cm^{-2})	Reference
Co$_9$S$_8$@Ni$_3$S$_2$/Ni foam	Seawater + KOH	154	36	173	100	[51]
ZnFe LDH@NiCoS/Ni foam	Seawater + KOH	284.8	–	85.7	10	[52]
CeOx@NiCo$_2$O$_4$/Ni foam	Simulated seawater	238	–	80	10	[53]
Co$_2$P-1/Ni$_2$P-1@Ni foam	KOH	310	–	69.9	10	[54]
Cu$_2$S@Ni$_3$S$_2$/Ni foam	seawater	78	6.6	63	10	[55]
SnO$_2$@MoS$_2$/Ni foam	KOH	290	11.52	42	50	[56]
CoCr LDH/NiO/Ni foam	KOH	253	1.99	70.92	50	[57]
NiSe$_2$@Fe-NiCoLDH/Ni foam	KOH	260	7.04	58.86	10	[58]
FeS/NiS/Ni foam	KOH	203	–	39	10	[59]
NiFe LDH@NiCoP/Ni foam	KOH	220	18.07	48.6	10	[60]
MoS$_2$@Ni(OH)$_2$/Ni foam	KOH	233	–	49	10	[61]
MgAlCe-LDH/β-Ni(OH)$_2$/Ni foam	Seawater	80	18.95	133	10	This work

shortest Tafel slope compared to the other three electrocatalysts, suggesting its superior OER kinetic dynamics [49].

Chronoamperometry measurements of the developed electrodes were performed to assess the electrodes' durability in the natural seawater electrolyte by employing a constant potential of 1.2 V vs. SCE for 1000 s, as demonstrated in Fig. 6f. Consequently, the recorded current density for the MgAlCe-LDH/β-Ni(OH)$_2$/Ni foam electrocatalyst was 1.24 times, 1.59 times, and 2.12 times greater than MgAlCe-LDH/Ni foam, β-Ni(OH)$_2$/Ni foam, and Ni foam, respectively. As shown in Fig. 6g, the EIS assessment of the constructed electrocatalysts was conducted in the natural seawater electrolyte, with frequency varying from 0.01 Hz to 100 kHz at a potential of 1.2 V vs. SCE. The ZView application was utilized to fit data and build the circuit for the Nyquist diagrams shown in Fig. 6g. Table 2 displays the data derived from the Nyquist diagram, which was recorded for the prepared electrodes for OER. As a consequence, the electrode conductivity of β-Ni(OH)$_2$/Ni foam, MgAlCe-LDH/Ni foam, and MgAlCe-LDH/β-Ni(OH)$_2$/Ni foam in seawater electrolyte is 2.95, 4.25, and 5.76 times larger than the conductivity of bare Ni foam, respectively. The smallest notable transmission of charge resistance (R$_{ct}$) for the MgAlCe-LDH/β-Ni(OH)$_2$/Ni foam compared to the three other electrodes confirms its better catalytic activity in OER. Similar funding is evident in the investigation conducted by Zhou et al. [50], which demonstrated that the Co$_4$Fe$_2$-LDHs/Co (OH)$_2$-NWs exhibited a considerably faster electron delivery mechanism during OER compared to Co(OH)$_2$/Ni foam which was attributed to the more extensive interlayer region of the Co$_4$Fe$_2$-LDHs/Co(OH)$_2$-NWs.

The outcomes of recent OER investigations with different electrolytes and catalysts supported on Ni foam is presented in Table 3.

3.4. HER performance of electrodes

In an N$_2$-saturated electrolyte (natural seawater), the electrocatalytic efficacy of Ni foam, β-Ni(OH)$_2$/Ni foam, MgAlCe-LDH/Ni foam, and MgAlCe-LDH/β-Ni(OH)$_2$/Ni foam toward HER was examined through a conventional three-electrode technique. Fig. 7a displays the LSV graphs of the developed electrodes for HER, with a scanning rate of 5 mV.s^{-1} and a potential area ranging from −1.2 to 0 V vs. SCE. The lowest overpotential of MgAlCe-LDH/β-Ni(OH)$_2$/Ni foam (337 mV) at a current density of 10 mA cm^{-2} in comparison to MgAlCe-LDH/Ni foam (369 mV), β-Ni(OH)$_2$/Ni foam (384 mV), and Ni foam (416 mV) confirms the enhanced electrocatalytic performance of MgAlCe-LDH/β-Ni(OH)$_2$/Ni foam toward HER. Liu et al. [62] observed comparable result regarding the enhanced catalytic activity in HER for Zr-doped CoFe-LDH/Ni foam compared to Ni foam and CoFe-LDH/Ni foam, indicating that the incorporation of Zr^{4+} into CoFe-LDH/NF can modify the electronic structure. As depicted in Fig. 7b, the HER performance of the Ni foam, β-Ni(OH)$_2$/Ni foam, MgAlCe-LDH/Ni foam, and MgAlCe-LDH/β-Ni(OH)$_2$/Ni foam electrocatalysts in the N$_2$-saturated seawater electrolyte was studied by CV curves at a −1.2 to 0 V vs. SCE potential range and at a scanning rate of 100 mV s^{-1}. According to recorded voltammograms in Fig. 7b, the MgAlCe-LDH/β-Ni(OH)$_2$/Ni foam electrode has a cathodic current density of −12 mA cm^{-2} at the smallest potential (−0.22 V vs. RHE) in comparison to MgAlCe-LDH/Ni foam (−13 mA cm^{-2}, -0.37 V vs. RHE), β-Ni(OH)$_2$/Ni foam (−6 mA cm^{-2}, -0.26 V vs. RHE), and Ni foam (−1 mA cm^{-2}, -0.25 V vs. RHE), showing the greatest electrocatalytic activity for HER. Fig. 7c shows the estimated C$_{dl}$ obtained from CV experiments at various scan rates for electrocatalysts during HER. Owing to the direct correlation between ECSA and C$_{dl}$, the highest C$_{dl}$ is achieved for MgAlCe-LDH/β-Ni(OH)$_2$/Ni foam (9.82 mF cm^{-2}), signifying its substantial electrochemically active surface in HER, in comparison to MgAlCe-LDH/Ni foam (8.21 mF cm^{-2}) and β-Ni(OH)$_2$/Ni foam (4.46 mF cm^{-2}). The lowest determined C$_{dl}$ for Ni foam (0.84 mF cm^{-2}) explains its diminished electrocatalytic activity in HER [45]. According to normalized LSV curves based on ECSA, in Fig. 7d, the superior electrochemical response of MgAlCe-LDH/β-Ni(OH)$_2$/Ni foam toward HER constant to three other electrocatalysts originates from its high inherent electrical conductivity [63]. As presented in Fig. 7e, the Tafel slopes for MgAlCe-LDH/β-Ni(OH)$_2$/Ni foam, MgAlCe-LDH/Ni foam, β-Ni(OH)$_2$/Ni foam, and Ni foam were obtained at about 33.63, 36.5, 38.29, and 43.26 mV.dec^{-1}, respectively. In accordance with the results collected, the lowest Tafel slope for the MgAlCe-LDH/β-Ni(OH)$_2$/Ni foam, in contrast with the other three electrocatalysts, indicates rapid kinetics and the highest electrocatalytic performance of the MgAlCe-LDH/β-Ni(OH)$_2$/Ni foam in HER [64]. Moreover, the endurability of the developed electrocatalysts during HER in N$_2$-saturated seawater was investigated by employing a steady potential of −1.2 V vs. SCE for 1000 s. As
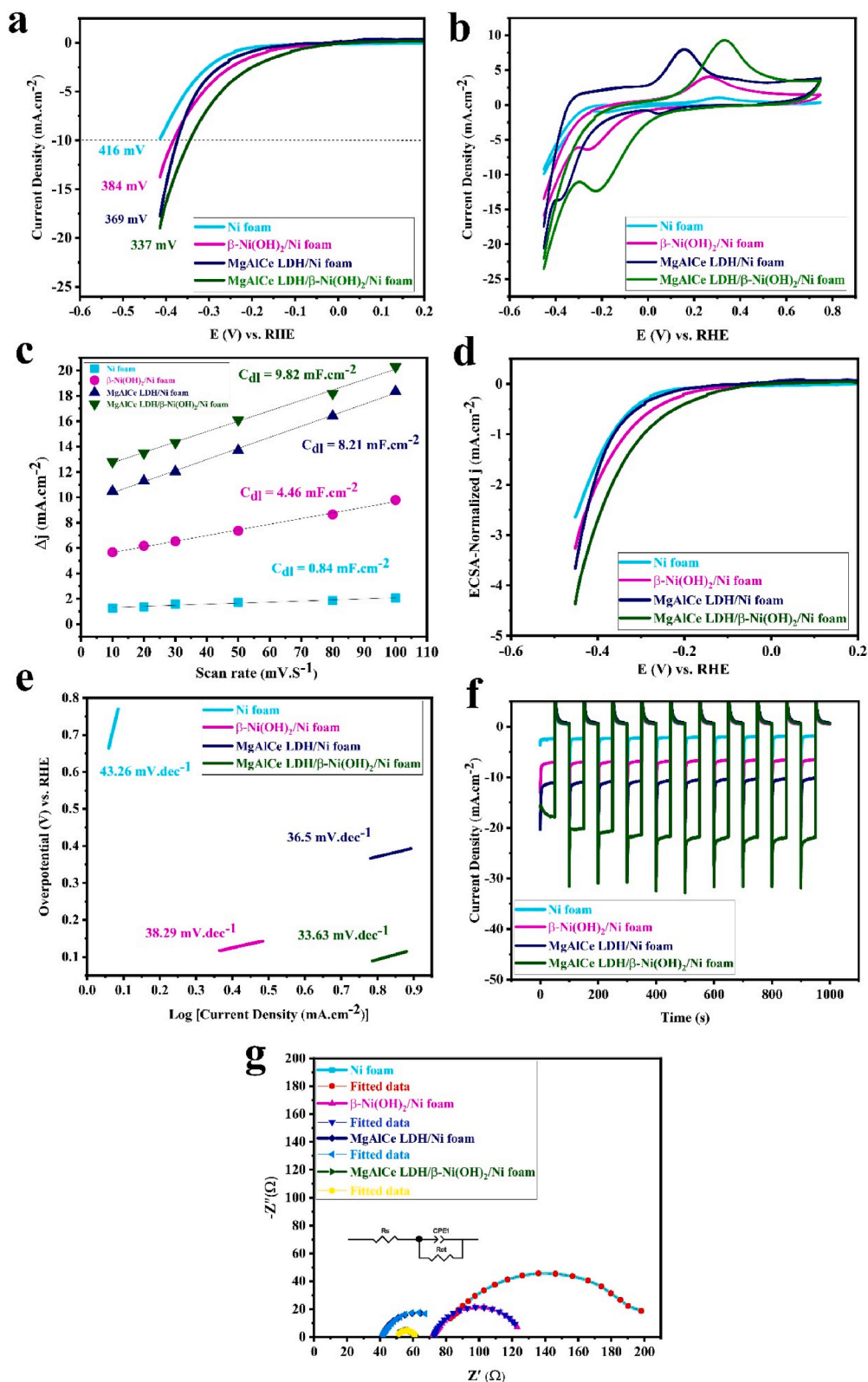
Fig. 7. LSV (a), CV (b), Cdl (c), ECSA-Normalized LSV (d), Tafel slope (e), chronoamperometry (f) and EIS (g) curves of the electrocatalysts for HER in N_2-saturated seawater electrolyte.

Table 4

The EIS fitting date of electrocatalysts for HER in seawater (pH = 8.2) electrolyte, with a potential of −1.2 V vs. SCE at room temperature.

Electrocatalysts	Rs (Ω)	CPE	R_{ct} (Ω)	Fitting error
Ni foam	75.94	0.75	132.3	0.008
β-Ni(OH)$_2$/Ni foam	72.72	0.86	52.88	0.008
MgAlCe-LDH/Ni foam	41.86	0.73	21.35	0.009
MgAlCe-LDH/β-Ni(OH)$_2$/Ni foam	50.79	0.92	10.46	0.007

Table 5

A contrasting view of the HER performance of distinct electrocatalysts supported on Ni foam.

Electrode	Electrolyte	Overpotential HER (mV)	Cdl (mF. cm^{-2})	Tafel slope (mV. dec^{-1})	Current density (mA. cm^{-2})	Reference
Ni-Sn/Ni foam	KOH	77	–	50	100	[66]
ZnFeLDH@NiCoS/Ni foam	Seawater + KOH	246.3	–	74.6	10	[52]
CeOx@NiCo$_2$O$_4$/Ni foam	Simulated seawater	144	–	160	10	[53]
Co$_2$P-1/Ni$_2$P-1@Ni foam	KOH	79	–	58.3	10	[54]
Cu$_2$S@Ni$_3$S$_2$/Ni foam	seawater	170	59	47	10	[55]
SnO$_2$@MoS$_2$/Ni foam	KOH	127	11.17	73.2	10	[56]
CoCr LDH/NiO/Ni foam	KOH	185	–	104.14	50	[57]
NiSe$_2$@Fe-NiCoLDH/Ni foam	KOH	130	4.29	108.9	10	[58]
FeS/NiS/Ni foam	KOH	144	–	120	10	[59]
NiFe LDH@NiCoP/Ni foam	KOH	120	17.41	88.2	10	[60]
MoS$_2$@Ni(OH)$_2$/Ni foam	KOH	134	11.3	35	10	[61]
MgAlCe-LDH/β-Ni(OH)$_2$/Ni foam	Seawater	337	9.82	33.63	10	This work
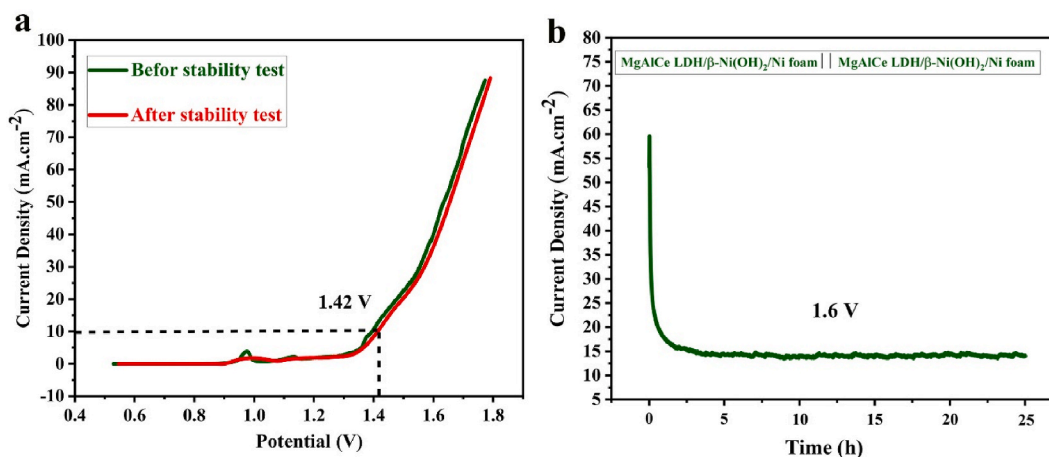
Fig. 8. LSV curve (a) and long-term stability test (b) of MgAlCe-LDH/β-Ni(OH)$_2$/Ni foam for overall seawater splitting.

illustrated in Fig. 7f, MgAlCe-LDH/β-Ni(OH)$_2$/Ni foam with a larger cathodic current density of about −25 mA cm^{-2} depicts better electrocatalytic activity for HER. Further to evaluate the electron transfer capability of the prepared electrocatalysts in HER, the EIS experiment was recorded at a frequency range of 0.01 Hz–100 KHz in a N$_2$-saturated seawater electrolyte at a potential of −1.2 V vs. SCE as demonstrated in Fig. 7g. Table 4 presents the data derived from the Nyquist diagram, which was recorded for the prepared electrodes during HER. According to Nyquist plots in Fig. 7g, the synthesis of β-Ni(OH)$_2$ on Ni foam led to a 2.49-fold decrease in the charge transfer resistance (R$_{ct}$) of the electrode compared with Ni foam in HER. On the other hand, the synthesis of MgAlCe-LDH on Ni foam caused a 6.19 times elimination in the Rct of the electrode compared to bare Ni foam in HER. Moreover, decorating MgAlCe-LDH on β-Ni(OH)$_2$/Ni foam caused a decrease of about 12.64 times in the resistance of the electrode to charge transmission during HER. The observed minimal Rct for the MgAlCe-LDH/β-Ni(OH)$_2$/Ni foam provides support of the effective electrical contact established between MgAlCe-LDH and β-Ni(OH)$_2$ on the Ni foam substrate that enhances electron transfer at the electrode surface, thereby boosting its electron conductivity [65].

Table 5 presents the results of current HER research using various electrolytes and catalysts.

Table 6
Recent water splitting studies using distinct electrolytes and electrocatalysts.

Electrode	Electrolyte	Cell voltage (V)	Stability time (h)	Reference
ZnFe LDH@NiCoS/Ni foam	Seawater + KOH	1.6	50	[52]
CeOx@NiCo$_2$O$_4$/Ni foam	Simulated seawater	1.66	60	[53]
Co$_2$P-1/Ni$_2$P-1@Ni foam	KOH	1.63	40	[54]
Cu$_2$S@Ni$_3$S$_2$/Ni foam	Seawater + KOH	1.6	15	[55]
SnO$_2$@MoS$_2$/Ni foam	KOH	1.57	300	[56]
CoCr LDH/NiO/Ni foam	KOH	1.57	60	[57]
NiSe$_2$@Fe-NiCoLDH/Ni foam	KOH	1.64	14	[58]
FeS/NiS/Ni foam	KOH	1.61	10	[59]
NiFe LDH@NiCoP/Ni foam	KOH	1.57	100	[60]
MoS$_2$@Ni(OH)$_2$/Ni foam	KOH	1.46	50	[61]
MgAlCe-LDH/β-Ni(OH)$_2$/Ni foam	Seawater	1.42	25	This work

3.5. Overall water splitting

As demonstrated in this work, the electrocatalytic performance of the MgAlCe-LDH/β-Ni(OH)$_2$/Ni foam electrode is superior to that of the MgAlCe-LDH/Ni foam, the β-Ni(OH)$_2$/Ni foam, and the Ni foam electrodes for both OER and HER. Hence, to study seawater electrolysis, a two-electrode arrangement with MgAlCe-LDH/β-Ni(OH)$_2$/Ni foam as the anode and the cathode was used [49]. Fig. 8a displays the LSV patterns obtained in a two-electrode configuration utilizing a natural seawater electrolyte, both prior to and subsequent to the stability assessments. Based on the documented LSV, the electrolyzer necessitates a voltage of 1.42 V to achieve a current density of 10 mA cm^{-2} in natural seawater. The long-term stability assessment of the electrocatalyst for total seawater splitting was conducted through chronopotentiometry measurements applying 1.6 V constant potential. The electrolyzer operated continuously for a duration of 25 h at a current density of 15 mA cm^{-2} within the seawater electrolyte, as depicted in Fig. 8b. The recorded LSV curve following 25 h of chronoamperometry demonstrates that MgAlCe-LDH/β-Ni(OH)$_2$/Ni foam functions as an effective bifunctional electrocatalyst. Table 6 provides a comparison of the generated cell voltage and stability of various electrodes throughout the total water splitting process in current studies.

4. Conclusion

To summarize, we have applied an easy procedure to produce β-Ni(OH)$_2$ on Ni foam at ambient temperature and then utilized a hydrothermal process to synthesize MgAlCe-LDH on the β-Ni(OH)$_2$/Ni foam substrate. Growing β-Ni(OH)$_2$ on Ni foam results in creating a rougher and electrocatalytically more active substrate and causes a decrease in the Tafel slope from 213 to 173 mV.dec^{-1} for OER and from 43.26 to 38.29 mV.dec^{-1} for HER. The lowest Tafel slope and the more rapid kinetics of the MgAlCe-LDH/β-Ni(OH)$_2$/Ni foam for both OER (133 mV.dec^{-1}) and HER (33.63 mV.dec^{-1}) compared to MgAlCe-LDH/Ni foam, β-Ni(OH)$_2$/Ni foam, and bare Ni foam in seawater electrolyte ensue from strong interaction and charge transfer capability between β-Ni(OH)$_2$ and MgAlCe-LDH. A two-electrode seawater-splitting arrangement employing MgAlCe-LDH/β-Ni(OH)$_2$/Ni foam electrocatalyst as the anode and cathode functions effectively, generating 10 mA cm^{-2} at a cell potential of 1.42 V.

CRediT authorship contribution statement

Mahsa Mehravaran: Writing – original draft, Validation, Methodology, Investigation, Data curation, Conceptualization. **Karim Asadpour-Zeynali:** Writing – review & editing, Supervision, Resources, Project administration, Conceptualization.

Data availability statement

Data will be made available on request.

Declaration of competing interest

The authors declare the following financial interests/personal relationships which may be considered as potential competing interests:The authors wish to thank the financial support from the University of Tabriz, Tabriz, Iran.

Acknowledgments

References

[1] S. Dokhani, M. Assadi, B.G. Pollet, Techno-economic assessment of hydrogen production from seawater, Int. J. Hydrogen Energy 48 (2023) 9592–9608.
[2] K.C. Majhi, M. Yadav, Bimetallic chalcogenide nanocrystallites as efficient electrocatalyst for overall water splitting, J. Alloys Compd. 852 (2021) 156736.

[3] I. Barauskienė, G. Laukaitis, E. Valatka, Stainless steel as an electrocatalyst for overall water splitting under alkaline and neutral conditions, J. Electroanal. Chem. 950 (2023) 117880.

[4] Y. Du, H. Qu, Y. Liu, Y. Han, L. Wang, B. Dong, Bimetallic CoFeP hollow microspheres as highly efficient bifunctional electrocatalysts for overall water splitting in alkaline media, Appl. Surf. Sci. 465 (2019) 816–823.

[5] L. Zhuang, S. Li, J. Li, K. Wang, Z. Guan, C. Liang, Z. Xu, Recent advances on hydrogen evolution and oxygen evolution catalysts for direct seawater splitting, Coatings 12 (2022) 050659.

[6] I. Ashraf, S. Ahmad, S. Rizwan, M. Iqbal, Fabrication of Ti$_3$C$_2$@MoO$_3$ nanocomposite as an electrode material for highly efficient and durable water splitting system, Fuel 299 (2021) 120928.

[7] A. Rezaei, Z. Karami, S. Aber, F. Feli, Oxygen Reduction Reaction Enhancement in Microbial Fuel Cell Cathode Using Cesium Phosphomolybdate Electrocatalyst, 2023, 129040.

[8] S. Jiang, Y. Liu, H. Qiu, C. Su, Z. Shao, High selectivity electrocatalysts for oxygen evolution reaction and anti-chlorine corrosion strategies in seawater splitting, Catalysts 12 (2022) 12030261.

[9] J. Chen, L. Zhang, J. Li, X. He, Y. Zheng, S. Sun, X. Fang, D. Zheng, Y. Luo, Y. Wang, J. Zhang, L. Xie, Z. Cai, Y. Sun, A.A. Alshehri, Q. Kong, C. Tang, X. Sun, High-efficiency overall alkaline seawater splitting: using a nickel-iron sulfide nanosheet array as a bifunctional electrocatalyst, J Mater Chem A Mater 11 (2022) 1116–1122.

[10] X. Guan, F.A. Chowdhury, N. Pant, L. Guo, L. Vayssieres, Z. Mi, Efficient unassisted overall photocatalytic seawater splitting on GaN-based nanowire arrays, J. Phys. Chem. C 122 (2018) 13797–13802.

[11] X. Hu, X. Tian, Y.W. Lin, Z. Wang, Nickel foam and stainless-steel mesh as electrocatalysts for hydrogen evolution reaction, oxygen evolution reaction and overall water splitting in alkaline media, RSC Adv. 9 (2019) 31563–31571.

[12] S. Jiang, H. Suo, T. Zhang, C. Liao, Y. Wang, Q. Zhao, W. Lai, Recent advances in seawater electrolysis, Catalysts 12 (2022) 12020123.

[13] G. Liu, Y. Xu, T. Yang, L. Jiang, Recent advances in electrocatalysts for seawater splitting, Nano Materials Science 5 (2023) 101–116.

[14] B. Xu, J. Liang, X. Sun, X. Xiong, Designing electrocatalysts for seawater splitting: surface/interface engineering toward enhanced electrocatalytic performance, Green Chem. 25 (2023) 3767–3790.

[15] Y. Li, X. Wu, J. Wang, H. Wei, S. Zhang, S. Zhu, Z. Li, S. Wu, H. Jiang, Y. Liang, Sandwich structured Ni$_3$S$_2$-MoS$_2$-Ni$_3$S$_2$@Ni foam electrode as a stable bifunctional electrocatalyst for highly sustained overall seawater splitting, Electrochim. Acta 390 (2021) 138833.

[16] A. Balčiūnaitė, K.K. Upadhyay, K. Radinović, D.M.F. Santos, M.F. Montemor, B. Šljukić, Steps towards highly-efficient water splitting and oxygen reduction using nanostructured β-Ni(OH)$_2$, RSC Adv. 12 (2022) 10020–10028.

[17] J.H. Yang, X. Xu, M. Chen, D. Yang, H. Lu, Y. Sun, C. Shao, Q. Song, J. Zhang, L. Gao, Y. Zhang, Morphology-controllable nanocrystal β-Ni(OH)$_2$/NF designed by hydrothermal etching method as high-efficiency electrocatalyst for overall water splitting, J. Electroanal. Chem. 882 (2021) 115035.

[18] Y. Cao, D. Zheng, S. Dong, F. Zhang, J. Lin, C. Wang, C. Lin, A composite corrosion inhibitor of MgAl layered double hydroxides Co-intercalated with hydroxide and organic anions for carbon steel in simulated carbonated concrete pore solutions, J. Electrochem. Soc. 166 (2019) C3106–C3113.

[19] J. Li, M. Luo, Z. Chen, E. Zhuang, B. Yu, Y. Chen, Y. Nong, Anti-corrosion mechanism of MgAl-LDHs inhibitors with varying anionic charge on reinforcing steel in simulated concrete pore solutions, Constr Build Mater 363 (2023) 129882.

[20] J. Liu, J. Wang, B. Zhang, Y. Ruan, L. Lv, X. Ji, K. Xu, L. Miao, J. Jiang, Hierarchical NiCo$_2$S$_4$@NiFe LDH Heterostructures Supported on Nickel Foam for Enhanced Overall-Water-Splitting Activity, 2017.

[21] K. Iqbal, A. Iqbal, A.M. Kirillov, B. Wang, W. Liu, Y. Tang, A new Ce-doped MgAl-LDH@Au nano catalyst for highly efficient reductive degradation of organic contaminants, J Mater Chem A Mater 5 (2017) 6716–6724.

[22] X. Xiong, D. Ding, D. Chen, G. Waller, Y. Bu, Z. Wang, M. Liu, Three-dimensional ultrathin Ni(OH)$_2$ nanosheets grown on nickel foam for high-performance supercapacitors, Nano Energy 11 (2015) 154–161.

[23] K. Iqbal, A. Iqbal, A.M. Kirillov, C. Shan, W. Liu, Y. Tang, A new multicomponent CDs/Ag@Mg-Al-Ce-LDH nanocatalyst for highly efficient degradation of organic water pollutants, J Mater Chem A Mater 6 (2018) 4515–4524.

[24] X. Shang, X. Li, W.H. Hu, B. Dong, Y.R. Liu, G.Q. Han, Y.M. Chai, Y.Q. Liu, C.G. Liu, In situ growth of Ni x S y controlled by surface treatment of nickel foam as efficient electrocatalyst for oxygen evolution reaction, Appl. Surf. Sci. 378 (2016) 15–21.

[25] Y. Wang, R. Zhu, Z. Wang, Y. Huang, Z. Li, Cu induced formation of dendritic CoFeCu ternary alloys on Ni foam for efficient oxygen evolution reaction, J. Alloys Compd. 880 (2021) 160523.

[26] E. Mohammadpour, K. Asadpour-Zeynali, α-Fe$_2$O$_3$@MoS$_2$ nanostructure as an efficient electrochemical catalyst for water oxidation, Microchem. J. 157 (2020) 104939.

[27] X. Xu, Y. Pan, Y. Zhong, L. Ge, S.P. Jiang, Z. Shao, From scheelite BaMoO$_4$ to perovskite BaMoO$_3$: enhanced electrocatalysis toward the hydrogen evolution in alkaline media, Compos. B Eng. (2020) 108214, 198.

[28] Y. Gao, T. Xiong, Y. Li, Y. Huang, Y. Li, M.S.J.T. Balogun, A simple and scalable approach to remarkably boost the overall water splitting activity of stainless steel electrocatalysts, ACS Omega 4 (2019) 16130–16138.

[29] P. Kour I. Deeksha, Sunny Ahmed, S.K. Sharma, K. Yadav, Y.K. Mishra, Transition metal-based perovskite oxides: emerging electrocatalysts for oxygen evolution reaction, ChemCatChem 15 (2023).

[30] X. Huo, H. Zhang, W. Shen, X. Miao, M. Zhang, M. Guo, Bifunctional aligned hexagonal/amorphous tungsten oxide core/shell nanorod arrays with enhanced electrochromic and pseudocapacitive performance, J Mater Chem A Mater 7 (2019) 16867–16875.

[31] H. Yan, D. Zhang, J. Xu, Y. Lu, Y. Liu, K. Qiu, Y. Zhang, Y. Luo, Solution growth of NiO nanosheets supported on Ni foam as high-performance electrodes for supercapacitors, Nanoscale Res. Lett. 9 (2014).

[32] Z. Qin, Y. Wang, X. Huang, W. Shen, J. Yu, J. Li, A facile synthesis of three dimensional β-Ni(OH)$_2$ composed of ultrathin nanosheets for high performance pseudocapacitor, J. Inorg. Organomet. Polym. Mater. 30 (2020) 2089–2097.

[33] X. Cao, L. Kong, Z. Gu, X. Xu, Ce and P123 modified layered double hydroxide (LDH) composite for the synthesis of polypropylene glycol monomethyl ether, RSC Adv. 12 (2022) 23183–23192.

[34] N. Ghanbari, H. Ghafuri, Preparation of novel Zn–Al layered double hydroxide composite as adsorbent for removal of organophosphorus insecticides from water, Sci. Rep. 13 (2023) 10215.

[35] G. Zheng, C. Wu, J. Wang, S. Mo, Y. Wang, Z. Zou, B. Zhou, F. Long, Facile synthesis of few-layer MoS2 in MgAl-LDH layers for enhanced visible-light photocatalytic activity, RSC Adv. 9 (2019) 24280–24290.

[36] X. Yi, H. Sun, N. Robertson, C. Kirk, Nanoflower Ni(OH)$_2$ grown in situ on Ni foam for high-performance supercapacitor electrode materials, Sustain. Energy Fuels 5 (2021) 5236–5246.

[37] A. Rezaei, H. Zarenezhad, S. Aber, R. Teimuri-Mofrad, Synergistic ORR catalysis: WS$_2$/CeO$_2$ composite in microbial fuel cells, Process Saf. Environ. Protect. 183 (2024) 1002–1012.

[38] S.N. Golovin, M.N. Yapryntsev, I.G. Ryltsova, A.A. Veligzhanin, O.E. Lebedeva, Novel cerium-containing layered double hydroxide, Chem. Pap. 74 (2020) 367–370.

[39] R. Pourfaraj, S.J. Fatemi, S.Y. Kazemi, P. Biparva, Synthesis of hexagonal mesoporous MgAl LDH nanoplatelets adsorbent for the effective adsorption of Brilliant Yellow, J. Colloid Interface Sci. 508 (2017) 65–74.

[40] M. Kostić, S. Najdanović, N. Velinov, M. Radović Vučić, M. Petrović, J. Mitrović, A. Bojić, Ultrasound-assisted synthesis of a new material based on MgCoAl-LDH: characterization and optimization of sorption for progressive treatment of water, Environ. Technol. Innov. 26 (2022) 102358.

[41] S. Min, X. Yang, A.Y. Lu, C.C. Tseng, M.N. Hedhili, L.J. Li, K.W. Huang, Low overpotential and high current CO$_2$ reduction with surface reconstructed Cu foam electrodes, Nano Energy 27 (2016) 121–129.

[42] X. Ma, Y. Chang, Z. Zhang, J. Tang, Forest-like NiCoP@Cu$_3$P supported on copper foam as a bifunctional catalyst for efficient water splitting, J Mater Chem A Mater 6 (2018) 2100–2106.

[43] Y. Wang, Q. Zhu, H. Zhang, Fabrication of β-Ni(OH)$_2$ and NiO hollow spheres by a facile template-free process, Chem. Commun. (2005) 5231–5233.

[44] S. Niu, Y. Sun, G. Sun, D. Rakov, Y. Li, Y. Ma, J. Chu, P. Xu, Stepwise electrochemical construction of FeOOH/Ni(OH)$_2$ on Ni foam for enhanced electrocatalytic oxygen evolution, ACS Appl. Energy Mater. 2 (2019) 3927–3935.

[45] H. Liu, R. Xie, Q. Wang, J. Han, Y. Han, J. Wang, H. Fang, J. Qi, M. Ding, W. Ji, B. He, W. Lü, Enhanced OER performance and dynamic transition of surface reconstruction in LaNiO$_3$ thin films with nanoparticles decoration, Adv. Sci. 10 (2023) 2207128.

[46] T. Periyasamy, S.P. Asrafali, A. Jang, S.C. Kim, J. Lee, Enhanced activity and stability of heteroatom-doped carbon/bimetal oxide for efficient water-splitting reaction, Polymers 15 (2023) 15173588.

[47] X. Yang, X. He, L. He, J. Chen, L. Zhang, Q. Liu, Z. Cai, C. Yang, S. Sun, D. Zheng, A. Farouk, M.S. Hamdy, Z. Ren, X. Sun, A hierarchical CuO nanowire@CoFe-layered double hydroxide nanosheet array as a high-efficiency seawater oxidation electrocatalyst, Molecules 28 (2023) 28155718.

[48] Y. Huang, L.W. Jiang, B.Y. Shi, K.M. Ryan, J.J. Wang, Highly efficient oxygen evolution reaction enabled by phosphorus doping of the Fe electronic structure in iron–nickel selenide nanosheets, Adv. Sci. 8 (2021) 2101775.

[49] J. Chen, L. Zhang, J. Li, X. He, Y. Zheng, S. Sun, X. Fang, D. Zheng, Y. Luo, Y. Wang, J. Zhang, L. Xie, Z. Cai, Y. Sun, A.A. Alshehri, Q. Kong, C. Tang, X. Sun, High-efficiency overall alkaline seawater splitting: using a nickel-iron sulfide nanosheet array as a bifunctional electrocatalyst, J Mater Chem A Mater 11 (2022) 1116–1122.

[50] L. Zhou, M. Guo, Y. Li, Q. Gu, W. Zhang, C. Li, F. Xie, D. Lin, Q. Zheng, One-step synthesis of wire-in-plate nanostructured materials made of CoFe-LDH nanoplates coupled with Co(OH)$_2$ nanowires grown on a Ni foam for a high-efficiency oxygen evolution reaction, Chem. Commun. 55 (2019) 4218–4221.

[51] Z. Zhao, H. Zhao, X. Du, X. Zhang, Ni$_3$S$_2$/Co$_9$S$_8$ directly grown on nickel foam as an environmentally friendly electrocatalyst for seawater splitting, Int. J. Hydrogen Energy 49 (2024) 811–822.

[52] M. Vedanarayanan, C.M. Chen, M.G. Sethuraman, Efficient hydrogen and oxygen evolution: dual-functional electrocatalyst of zinc iron layered double hydroxides and nickel cobalt sulfides on nickel foam for seawater splitting, ACS Appl. Energy Mater. 7 (2024) 7260–7271.

[53] W. Liu, J. Zhao, L. Dai, Y. Qi, K. Liang, J. Bao, Y. Ren, Interface engineering overall seawater splitting of self-supporting CeOx@NiCo$_2$O$_4$ arrays, Inorg. Chem. 63 (2024) 6016–6025.

[54] H. Zhao, J. Liang, Y. Zhao, Construction of hierarchical Co$_2$P/Ni$_2$P heterostructures on Ni foam as efficient bifunctional electrocatalyst for overall water splitting, J. Alloys Compd. 907 (2022) 164479.

[55] Z. Zhao, H. Zhao, X. Du, X. Zhang, Controllable preparation of Cu$_2$S@Ni$_3$S$_2$ grown on nickel foam as efficient seawater splitting electrocatalyst, Int. J. Hydrogen Energy 49 (2024) 1528–1537.

[56] W. He, L. Wang, H. Zhang, S. Gao, W. Yu, D. Yin, X. Dong, SnO$_2$@MoS$_2$ heterostructures grown on nickel foam as highly efficient bifunctional electrocatalyst for overall water splitting in alkaline media, J. Alloys Compd. 938 (2023) 168678.

[57] S. Singha Roy, R. Madhu, K. Bera, S. Nagappan, H.N. Dhandapani, A. De, S. Kundu, Tuning the activity and stability of CoCr-LDH by forming a heterostructure on surface-oxidized nickel foam for enhanced water-splitting performance, ACS Appl. Mater. Interfaces 16 (2024) 5965–5976.

[58] Q. Wang, C. Wang, X. Du, X. Zhang, Synthesis of NiSe$_2$@M (M=Cu, Fe and Zn)–NiCo LDH with porous structure on nickel foam for overall fresh and seawater splitting, Int. J. Hydrogen Energy 51 (2024) 1154–1166.

[59] R. Zhang, Z. Zhu, J. Lin, K. Zhang, N. Li, C. Zhao, Hydrolysis assisted in-situ growth of 3D hierarchical FeS/NiS/nickel foam electrode for overall water splitting, Electrochim. Acta 332 (2020) 135534.

[60] H. Zhang, X. Li, A. Hähnel, V. Naumann, C. Lin, S. Azimi, S.L. Schweizer, A.W. Maijenburg, R.B. Wehrspohn, Bifunctional heterostructure assembly of NiFe LDH nanosheets on NiCoP nanowires for highly efficient and stable overall water splitting, Adv. Funct. Mater. 28 (2018) 1706847.

[61] C. Wei, C. Liu, L. Gao, Y. Sun, Q. Liu, X. Zhang, J. Guo, MoS$_2$ nanosheets decorated Ni(OH)$_2$ nanorod array for active overall water splitting, J. Alloys Compd. 796 (2019) 86–92.

[62] W. Liu, K. Jiang, Y. Hu, Q. Li, Y. Deng, J. Bao, Y. Lei, Zr-doped CoFe-layered double hydroxides for highly efficient seawater electrolysis, J. Colloid Interface Sci. 604 (2021) 767–775.

[63] S. Wang, J. Wu, J. Yin, Q. Hu, D. Geng, L.M. Liu, Improved electrocatalytic performance in overall water splitting with rational design of hierarchical Co$_3$O$_4$@NiFe layered double hydroxide core-shell nanostructure, Chemelectrochem 5 (2018) 1357–1363.

[64] E. Mohammadpour, K. Asadpour-Zeynali, ZnFe$_2$O$_4$@ZnFe$_2$S$_4$ core-shell nanosheet on Ni foam as efficient and novel electrocatalyst for oxygen generation, Int. J. Hydrogen Energy 46 (2021) 26940–26949.

[65] J. Wang, G. Lv, C. Wang, A highly efficient and robust hybrid structure of CoNiN@NiFe LDH for overall water splitting by accelerating hydrogen evolution kinetics on NiFe LDH, Appl. Surf. Sci. 570 (2021) 151182.

[66] J.D. Gojgić, A.M. Petričević, T. Rauscher, C.I. Bernäcker, T. Weißgärber, L. Pavko, R. Vasilić, M.N. Krstajić Pajić, V.D. Jović, Hydrogen evolution at Ni foam electrodes and Ni-Sn coated Ni foam electrodes, Appl. Catal. Gen. 663 (2023) 119312.